



Cite this: DOI: 10.1039/c8nr01397g

## Hierarchical nanopores formed by block copolymer lithography on the surfaces of different materials pre-patterned by nanosphere lithography†

Katharina Brassat,<sup>a</sup> Daniel Kool,<sup>a,b</sup> Julius Bürger<sup>a,b</sup> and Jörg K. N. Lindner<sup>a,b</sup>

Bottom-up patterning techniques allow for the creation of surfaces with ordered arrays of nanoscale features on large areas. Two bottom-up techniques suitable for the formation of regular nanopatterns on different length scales are nanosphere lithography (NSL) and block copolymer (BCP) lithography. In this paper it is shown that NSL and BCP lithography can be combined to easily design hierarchically nanopatterned surfaces of different materials. Nanosphere lithography is used for the pre-patterning of surfaces with antidots, *i.e.* hexagonally arranged cylindrical holes in thin films of Au, Pt and TiO<sub>2</sub> on SiO<sub>2</sub>, providing a periodic chemical and topographical contrast on the surface suitable for templating in subsequent BCP lithography. PS-*b*-PMMA BCP is used in the second self-assembly step to form hexagonally arranged nanopores with sub-20 nm diameter within the antidots upon microphase separation. To achieve this the microphase separation of BCP on planar surfaces is studied, too, and it is demonstrated for the first time that vertical BCP nanopores can be formed on TiO<sub>2</sub>, Au and Pt films without using any neutralization layers. To explain this the influence of surface energy, polarity and roughness on the microphase separation is investigated and discussed along with the wetting state of BCP on NSL-pre-patterned surfaces. The presented novel route for the creation of advanced hierarchical nanopatterns is easily applicable on large-area surfaces of different materials. This flexibility makes it suitable for a broad range of applications, from the morphological design of biocompatible surfaces for life science to complex pre-patterns for nanoparticle placement in semiconductor technology.

Received 16th February 2018,  
Accepted 24th April 2018

DOI: 10.1039/c8nr01397g

rsc.li/nanoscale

## Introduction

Block copolymer (BCP) lithography is an emerging self-organization technique for large-area surface patterning with nanoscale motifs.<sup>1,2</sup> Thin films patterned with regular arrays of features with sizes of a few to a few tens of nanometers can be easily created by BCP lithography. Such nanopatterns find applications in many fields such as magnetic storage media,<sup>3,4</sup> fin-field effect transistors,<sup>5</sup> seeds for nanowire growth,<sup>6,7</sup> or quantum dots.<sup>8,9</sup> Hierarchical nanopatterns are of particular interest in nanotechnologies as they provide a link between

the micro- and nanoworld. Designed hierarchically patterned material surfaces allow for the precise positional control of nanoscale features and exhibit flexibility in pattern shape and size. The surface patterning with self-assembly techniques makes such patterns easily accessible on large areas, which is a prerequisite for the use of tailored surfaces in real world applications. For this, however, a detailed understanding of the self-organization driving forces and interfacial interactions is necessary.

In BCP lithography the self-induced microphase separation of block copolymers into well-defined self-organized motifs is the major driving force, leading to a minimization of the BCP free energy  $F_{\text{mix}}$ .<sup>10–12</sup> Block copolymers consist of two blocks of different polymer species A and B which are covalently bonded to each other. In a thin film as well as bulk material the molecules form an intricate network without medium or long range order. Order is induced by giving the BCP molecules mobility by annealing above the glass temperature, a process leading to so-called microphase separation. Due to repulsive forces between the blocks, areas enriched with either one or the other polymer-species evolve, minimizing interfacial energies

<sup>a</sup>Dept. of Physics, Paderborn University, Warburgerstr. 100, 33098 Paderborn, Germany. E-mail: katharina.brassat@upb.de, lindner@physik.upb.de

<sup>b</sup>Center for Optoelectronics and Photonics Paderborn (CeOPP), Warburgerstr. 100, 33098 Paderborn, Germany

† Electronic supplementary information (ESI) available: Large-area SEM image; SEM images of Pt antidots with in-lens and BSE detectors; SEM image of nanopores in Ti antidots with sputtered Pt; Au antidots with spincoated polymer prior to annealing; geometrical estimation of dome formation. See DOI: 10.1039/c8nr01397g

between these homopolymer domains. Provided that the tendency to undergo microphase separation (expressed by the Flory–Huggins parameter<sup>13</sup>) and the polymer chain length is large enough,<sup>12</sup> the areas can form different motifs depending on the block length ratio between blocks A and B. A phase diagram predicts *e.g.* lamellar regions of blocks A and B for polymers with 50% fractions of A and B or hexagonally arranged cylinders of A in a matrix of B for a 30/70% ratio.<sup>14</sup>

For nanopatterning of surfaces, BCP lithography is exploited in thin polymer films on solid substrates. Once microphase separation has been accomplished, one of the polymers can be selectively removed in a solvent, leaving a topographic nanopattern of the remaining polymer type behind.<sup>14–16</sup> This process step works particularly well if the BCP motifs (lamellae or cylinders) sit vertically oriented on the substrate surface,<sup>1,17,18</sup> which for surface patterning purposes is a preferable situation. A well investigated example is the formation of nanoporous polystyrene (PS) films by microphase separation of polystyrene-*b*-polymethyl-methacrylate (PS-*b*-PMMA) BCP with 70% to 30% block length ratio into hexagonally arranged PMMA cylinders in a PS matrix.<sup>1</sup> Removal of the PMMA cylinders leads to a PS film with empty cylindrical pores, the diameter and the next neighbor distance of which are determined by the molecular weight of the BCP.

In thin films the interfaces with the substrate on one side and air on the other side affect the microphase separation process crucially as they contribute to the free energy of the BCP.<sup>17</sup> The total free energy  $F$  of the BCP thin film can be expressed by a phenomenological description:<sup>17</sup>

$$F = F_{\text{mix}} + F_{\text{elast}} + F_{\text{interface}}. \quad (1)$$

$F_{\text{mix}}$  describes the interactions within the BCP, *i.e.* repulsive forces between polymer species described by the Flory–Huggins parameter as a function of the polymerization degree and block length ratio, resulting in microphase separation as stated above. In the following discussions this energy will be considered as constant as long as the same PS-*b*-PMMA BCP is used.  $F_{\text{elast}}$  describes the elastic free energy of the stretched polymer chains including their conformation.<sup>17</sup> This energy contribution is discussed later in this paper to balance surface inhomogeneities by changing the characteristic dimensions of the microphase separated homopolymer domains.  $F_{\text{interface}}$  includes interactions at all interfaces between the polymer-species A and B, the air and a solid substrate.  $F_{\text{interface}}$  determines the surface wetting with the polymer and affects the orientation of the microphase separated homopolymer domains.

Interactions between polymer and substrate or polymer and air can lead to a preferential wetting of the substrate with one or the other polymer blocks of the BCP, resulting in different orientations of PMMA cylinders with respect to the surface. A surface is said to be “neutral” to both polymer types A and B if there is no preferential wetting with one polymer species.<sup>19</sup> This is the case if the interfacial energies  $\sigma_{\text{substrate-A}}$  and  $\sigma_{\text{substrate-B}}$  between the substrate surface and polymers A and B,

respectively, are commensurate. However, if the surface is not “neutral” but shows an affinity to polymer A, *i.e.*  $\sigma_{\text{substrate-A}} < \sigma_{\text{substrate-B}}$ , microphase separation will lead to an arrangement of blocks in which the contact area of the surface with block A is maximized. The interface between polymer and air is commonly considered to be “neutral” and is kept constant throughout this work. The use of different substrates, however, will be shown to influence the microphase separation crucially. For cylinder-forming PS-*b*-PMMA BCP, the surface needs to be “neutral” with regard to both polymer types A and B in order to obtain a vertical orientation of PMMA cylinders on the surface. A non-neutral surface leads to a PMMA cylinder orientation parallel to the substrate surface. Such surface-parallel cylinders arrange then in the form of “fingerprint” patterns due to the lack of long-range order.

To control the formation of ordered, well-oriented nanopatterns with well-defined orientation with respect to the surface it is thus crucial to control the wetting behavior of polymer blocks on the substrate surface, *i.e.* to adjust the surface free energies (SFE) at the interface between the polymer blocks and the substrate.<sup>20,21</sup> To this end, surfaces can *e.g.* be modified by functionalization with self-assembled monolayers of chlorosilanes<sup>22</sup> or by X-ray or UV/ozone exposure<sup>23,24</sup> to make the surface homogeneously neutral to both BCP blocks. A particularly common approach is the deposition of a random copolymer (RCP) brush layer as a neutralizing interfacial layer.<sup>18,24–28</sup> The RCP typically consists of the same polymer species A and B as the BCP but with monomer units being randomly arranged in the polymer chains. One end of the polymer chain typically contains a hydroxy group which can covalently bind to (oxide) surfaces. Thus, the RCP polymer chain will stretch away from the substrate surface and build a dense brush layer. Due to the random sequence of A and B blocks in the RCP this leads to a random surface termination with the two monomers A and B providing a neutral surface for the A-*b*-B BCP. The deposition of a RCP brush layer today is a standard process step in order to obtain vertical cylinder patterns in BCP lithography.<sup>17,29–31</sup>

In order to control the arrangement and orientation of BCP nanopatterns, to improve their long-range order, to arrange blocks into new motifs and to pinpoint their placement on a substrate, it has been suggested to use directed block copolymer self-assembly. Impressive results have been presented *e.g.* by the groups of Ross and Berggren<sup>32</sup> or Kim.<sup>33</sup> To this end, surfaces are chemically or topographically pre-patterned prior to BCP deposition and microphase separation.<sup>34–38</sup> Polymers then again interact with these pre-patterns and arrange themselves during microphase separation into motifs, the arrangement of which is guided by the template. However, pre-patterning of the surface adds more complexity to the interfacial energies determining the self-ordering process.

Typically, substrate pre-patterning is done by conventional electron beam lithography (EBL). Electron beam lithography provides a high resolution, which is indispensable for the pre-patterning with feature sizes similar to the size of BCP motifs, *i.e.* a few to a few tens of nanometers. Both, trenches in the

substrate surface and nanoposts on the substrate surface, have been used for the introduction of a long range order of BCP patterns.<sup>39</sup> A drawback of EBL is that this technique uses sequential pattern writing under vacuum conditions, which is costly and time consuming and therefore not applicable if large surface areas are to be structured. The precision and flexibility of EBL, however, is not always needed. Pre-patterning can also be done using features substantially larger than the features of BCP lithography. In terms of pattern density multiplication,<sup>40</sup> a pre-pattern density which is a factor of 34 smaller than the BCP nanopattern density<sup>41</sup> can be sufficient to have a guiding effect on the BCP self-arrangement. Such larger features can be conveniently fabricated using other well-established bottom-up techniques which are scalable to large surface areas, as we will show in this paper. By combining self-organizing techniques which operate at different length scales it becomes possible to achieve hierarchical nanopatterns designed by a coarse self-organized pre-pattern and a finer nanopattern created by BCP lithography.

The technique which we are proposing here for the pre-patterning is nanosphere lithography (NSL).<sup>42</sup> In NSL, nanospheres from a colloidal suspension are deposited onto a substrate to form a hexagonally close-packed mono- or double layer by self-organization.<sup>43</sup> These layers can be fabricated on large areas. They then act as shadow masks in a subsequent material deposition step. Particles consisting of the deposited material and in the shape of the projected mask openings remain on the substrate after sphere mask removal. By using *e.g.* simple sphere monolayers, arrays of nanoparticles with a triangular footprint can be created. For the preparation of different motifs, the shape of the shadow mask openings can be modified.<sup>43,44</sup> In particular, the use of polymer spheres for NSL allows for an easy sphere mask modification<sup>45–47</sup> *e.g.* by thermal, ion beam or plasma treatment.<sup>48–51</sup> A treatment of polymer spheres in an oxygen/argon plasma, for instance, results in the shrinkage of spheres. The resulting arrangement of non-interconnected spheres leaves a larger fraction of the substrate unmasked. In a subsequent material deposition step, this allows for the creation of material thin films with regular dots of free substrate. These so-called antidot patterns provide a topographical and chemical patterning of a surface, which makes them suitable for many applications *e.g.* in electrooptics or bionanotechnology, as we have shown previously.<sup>52,53</sup>

In this paper we show for the first time how hierarchical nanopores can be created on large-area surfaces by combining nanosphere lithography as a pre-patterning technique with block copolymer lithography.

So far, BCP lithography has been well investigated on SiO<sub>2</sub> surfaces by many groups. However, barely any investigation of the BCP lithography performed on other materials can be found in the literature.<sup>54</sup> In the first part of this paper, we demonstrate the nanopore formation on surfaces of materials other than SiO<sub>2</sub>, *i.e.* TiO<sub>2</sub>, Au and Pt, and discuss the need for neutralization layers such as RCP brushes on these surfaces. For a better understanding of the interactions between the material surfaces and the BCP, surface energies are deter-

mined by contact angle measurements and we discuss the effect of surface polarity on the BCP microdomain orientation. Also, the influence of surface roughnesses on the nanopore formation is shown.

The patterning of thin films of the above materials is introduced in the second part of this paper. Nanosphere lithography is used for the creation of antidot-patterns, *i.e.* cylindrical hole arrays in the metal/metal oxide thin films, which exhibit a topographical and chemical surface pattern with periodicities of a few hundreds of nanometers. We show that such pre-patterns allow for the creation of hierarchical nanostructures when combined with sub-20 nm patterning by block copolymer lithography. We discuss the influence of the antidot film material and the antidot topography on the block copolymer lithography.

We present for the first time how the combination of these two self-assembly techniques and the choice of the antidot film material allow for a site-selective nanopore formation, and we discuss the influence of the wetting state on the self-ordering process for such materials systems.

## Experimental

### Thin film deposition

Planar metal thin films are deposited on Si (100) surfaces by different physical vapor deposition (PVD) techniques. Prior to deposition the Si crystals with their native oxide layer were cleaned in an oxygen plasma using an Oxford Instruments PlasmaLab 80plus instrument. For the electron beam evaporation of pure titanium, gold and platinum films a home-made deposition system operating at a base pressure of about  $5 \times 10^{-6}$  mbar was used. Film thicknesses were controlled by a quartz microbalance and set to 15–30 nm. To improve the adhesion of Au films, 2 nm of Ti was evaporated prior to Au deposition without breaking the vacuum. In the case of pure Ti films, no special care was taken to avoid the formation of a native oxide film. Thus in the following we consider the surface of these films to consist of TiO<sub>2</sub>.

35 nm thin films of gold and platinum were also deposited by sputter deposition in an ISI PS-2 coating unit at 1.2 kV and 20  $\mu$ A under an argon atmosphere of 0.1 mTorr.

### Antidot preparation

Topographic pre-patterning of thin films on SiO<sub>2</sub>/Si surfaces is done by means of nanosphere lithography as depicted in Fig. 1(a). Monolayers of polymer spheres are deposited on oxygen plasma cleaned Si surfaces by convective self-assembly. To this end, a droplet of an aqueous suspension of polystyrene spheres with a diameter of 618 nm (CV < 3%, 2 wt% solid fraction, Thermo Scientific Inc.) is pipetted onto the substrate and subsequently moved across the surface with a doctor blade at a constant velocity. Due to evaporation fluxes of the liquid at the contact line between the droplet and the substrate, PS spheres are transported towards the liquid meniscus and capillary forces between the spheres lead to a hexagonally close-packed

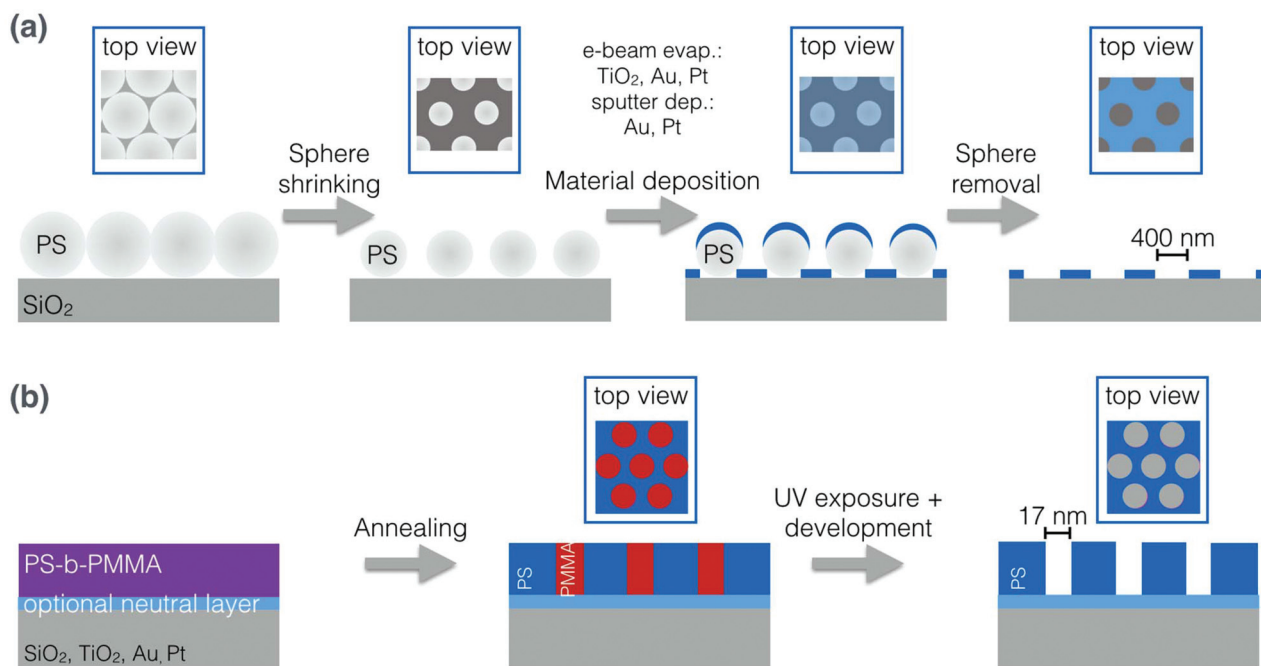


**Fig. 1** Sketch of the experimental procedures of (a) antidot pattern preparation and (b) block copolymer lithography. (a) From left to right: A hexagonally close-packed monolayer of polystyrene (PS) spheres is deposited onto the substrate. PS spheres are then shrunk in a reactive ion etching process and used as a shadow mask in a material deposition step (electron beam evaporation of  $\text{TiO}_2$ , Au or Pt or sputter deposition of Au or Pt). After sphere removal an antidot patterned thin film remains. (b) From left to right: Thin films of the PS-*b*-PMMA block copolymer are spin coated onto the substrate, a RCP-covered or uncovered thin film of  $\text{SiO}_2$ ,  $\text{TiO}_2$  or electron beam evaporated or sputter deposited Au or Pt on Si (not shown). Annealing of the thin film leads to microphase separation of the polymer, here into PMMA cylinders in a PS matrix. By UV exposure and development PMMA cylinders can be selectively removed; a regular array of vertical cylindrical nanopores in the PS matrix remains.

arrangement of the spheres in a monolayer. These PS sphere monolayers are subsequently modified by reactive ion etching in an Oxford Instruments PlasmaLab 80plus instrument. The treatment in a plasma with 2 sccm  $\text{O}_2$  and 8 sccm Ar at 75 mTorr with 50 W RF power for 5 min leads to a shrinking of the 618 nm polymer spheres to a mean diameter of 415 nm. The shrunk sphere arrays act then as a shadow mask during a material deposition step. Gold, titanium and platinum are deposited by both, electron beam evaporation and sputtering, as stated above for the planar thin films. The sphere masks are finally removed by dissolution in tetrahydrofuran in an ultrasonic bath. This procedure results in the formation of a thin film with a hexagonal arrangement of circular openings, which penetrate down to the  $\text{SiO}_2$  surface. We call these film openings antidots.<sup>52,53</sup>

### Block copolymer lithography

A poly(styrene-*b*-methylmethacrylate) (PS-*b*-PMMA) block copolymer with a molecular weight  $M_n$  of 67 kg mol<sup>-1</sup> (PDI = 1.09, purchased from Polymer Source Inc.) with a polystyrene fraction of 68.7% is used for BCP lithography. The experimental procedure is shown in Fig. 1(b). Thin films with a thickness of 30 nm are deposited by spin coating a 0.8 wt% polymer solution in toluene. The samples are then annealed at a temperature of 180 °C for 24 h at a pressure of  $3 \times 10^{-3}$  mbar for microphase separation. The microphase separation leads to the for-

mation of hexagonally arranged PMMA cylinders in a PS matrix. For selective removal of PMMA cylinders the microphase separated films are exposed to UV light with a spectral maximum at 254 nm for 20 minutes and developed in acetic acid for 30 minutes leaving the nanoporous PS film.

This procedure is performed on  $\text{SiO}_2$  and  $\text{TiO}_2$  surfaces as well as sputter and electron beam evaporation deposited thin films of Au and Pt. The same procedure was used to deposit nominally 30 nm thick BCP films on antidot films of the same materials (part B of the Results section). For the partition of BCP volume fractions within the antidots and on the rims between them, see the ESI (Fig. S4†).

Some of the  $\text{SiO}_2$  and  $\text{TiO}_2$  surfaces were coated with a PS-*co*-PMMA random copolymer (RCP) neutralization layer prior to the deposition of the PS-*b*-PMMA block copolymer. The RCP forms a molecular brush layer on the substrate surface and is commonly used in the literature to promote a PMMA cylinder orientation perpendicular to the substrate surface during microphase separation on  $\text{SiO}_2$  substrates.<sup>10</sup> For the preparation of such a neutralization layer, we use the random copolymer poly(styrene-*co*-methyl methacrylate) with  $\alpha$ -hydroxy and  $\omega$ -TEMPO-moiety termination ( $M_n = 5.3$  kg mol<sup>-1</sup>; PDI = 1.44; 74 mol% PS-content, purchased from Polymer Source Inc.). An approximately 60 nm thick layer of the RCP dissolved in toluene with a concentration of 2 wt% is spin coated onto the substrate surface. This layer is then annealed at 140 °C for

48 h at  $3 \times 10^{-3}$  mbar, resulting in the brush layer formation. After annealing the unbonded polymer is removed by rinsing with toluene and the block copolymer is immediately deposited on the top and processed as described above.

### Characterization methods

The substrate surfaces are characterized prior to BCP lithography by means of atomic force microscopy (AFM) and contact angle measurements. A Digital Instruments Dimension 3100 Series Scanning Probe Microscope AFM is used in contact mode for the measurement of the surface roughness. Contact angles with water, diiodomethane and ethylene glycol (analytical grade, Sigma Aldrich) are measured with a Krüss Drop Shape Analyzer DSA25E in the sessile drop mode. Test liquid droplets with a volume of 2  $\mu\text{l}$  are deposited on the surface and the measured drop contour is fitted with an ellipse fit. By means of the OWRK method,<sup>55</sup> polar and disperse fractions of the surface free energies are calculated from the contact angles.

The nanoporous PS films on different substrates are investigated by scanning electron microscopy (SEM) (Zeiss Ultra Plus) at an acceleration voltage of 2 kV using an in-lens detector. The images are analyzed with Delaunay triangulation based software<sup>56,57</sup> to determine the quality of the nanopore arrangement with respect to pore densities. Pore size distributions are determined from SEM images using an intensity thresholding technique. Typically, average pore densities were determined on areas of 8  $\mu\text{m}^2$  containing about 7600 pores; pore diameter distributions were calculated by evaluating about 2700 pores on areas of 3  $\mu\text{m}^2$ .

Cross-sectional samples for transmission electron microscopy (TEM) were prepared using mechanical sample cutting and thinning followed by an eventual low-energy ion milling step, similar to standard techniques used in the field. In order to protect the BCP film and in order to enhance contrasts of the pores, 10 nm of Ni was evaporated prior to the specimen preparation. Finished TEM specimens were analyzed at 200 kV in bright-field TEM mode with the new JEOL ARM 200 F analytical  $c_s$ -corrected TEM at the University of Paderborn (OWL-Analytic Centre).

## Results and discussion

### BCP lithography on different planar surfaces

**Material impact.** The influence of the substrate surface chemistry on the microphase separation is studied on planar thin films using SEM imaging as shown in Fig. 2. To this end, both  $\text{SiO}_2$  and  $\text{TiO}_2$  surfaces were used, either covered (left column) or not covered (right column) with a RCP brush layer, as illustrated schematically in Fig. 2(a) and (b). Fig. 2(c) shows the result of BCP lithography performed with a PS-*b*-PMMA BCP containing 70% PS on a neutralized  $\text{SiO}_2$  surface. In agreement with the results of many other groups for this material combination,<sup>1</sup> the PMMA has formed upon annealing a hexagonal array of cylinders standing vertically on the  $\text{SiO}_2$

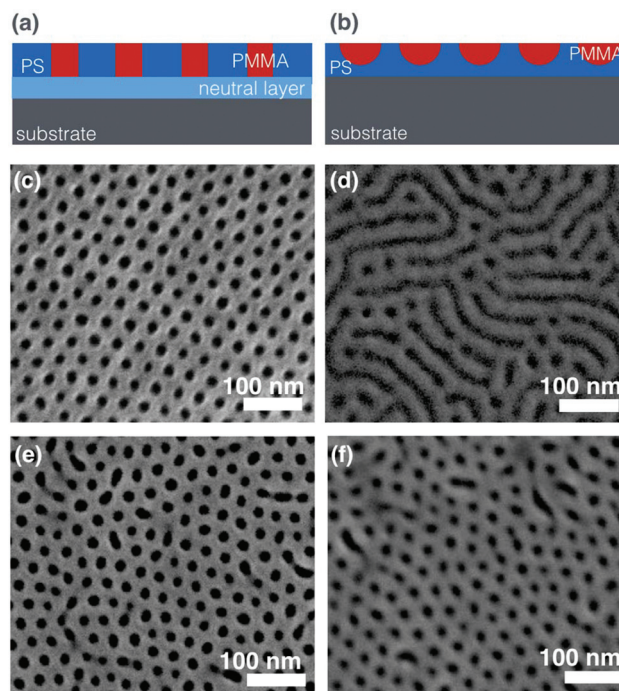


**Fig. 2** Influence of surface pre-treatment on PMMA cylinder orientation during BCP lithography. Cross-sectional sketch of PMMA cylinder orientation on a neutral surface perpendicular to the substrate (a) or on a non-neutral surface in parallel (b). Top view SEM images of nanoporous PS films on  $\text{SiO}_2$  surfaces with a neutralisation layer (c) and without a neutral layer (d). SEM images of PS films on  $\text{TiO}_2$  surfaces with (e) and without (f) a neutral layer.

surface. After exposure to UV light and treatment with acetic acid, only the PS matrix (grey) remains on the substrate surface and contains nanopores, which are visible as dark dots at the position of the former PMMA cylinders. The nanopores have a mean diameter of  $16.8 \pm 2.9$  nm (standard deviation) and are hexagonally arranged with a mean distance between pore centers of  $35.0 \pm 5.0$  nm. These sizes are determined by the molecular weight of the BCP used. The density of pores gives information about the pattern homogeneity: the higher the pore density the more regular is the pore arrangement. High densities at a narrow size distribution can only be achieved if the microphase separation of PS and PMMA is complete and only a few defects occur. Typical defects in such an arrangement are grain boundaries which come along with pore coordinations differing from six for perfect hexagonal arrangements. In Fig. 2(c), the pore density is  $9.4 \times 10^{10} \text{ cm}^{-2}$ , which matches the geometrical maximum of  $9.43 \times 10^{10} \text{ cm}^{-2}$ .

The formation of round looking nanopores by BCP lithography requires the control of PMMA cylinder orientation perpendicular to the surfaces. Two extreme orientations, cylinders oriented parallel or perpendicular to the substrate surface, are shown in the sketches in Fig. 2(a and b). PMMA cylinders are perpendicularly oriented to the surface (Fig. 2(a)) if the interfaces with the substrate and the gas environment are neutral, *i.e.* energetically equal for both BCP polymer species A and

B. The cylinders are oriented parallel within the layer if the interfaces are not neutral, to maximize the contact areas with one polymer species like in Fig. 2(b) explained above.

SiO<sub>2</sub> surfaces are not neutral as is visible from their different wettability with PS and PMMA. This results in PMMA cylinders which are oriented parallel to the substrate interface if no RCP brush layer is used, as shown in Fig. 2(d). Only by a modification of the SiO<sub>2</sub> surface with a random copolymer brush the PMMA cylinders can be guided to be perpendicular to the surface (Fig. 2(c)).

We performed the BCP lithography also on a TiO<sub>2</sub> surface with and without RCP. The results are shown in Fig. 2(e) for BCP lithography with the RCP neutral layer and in Fig. 2(f) for a sample without the RCP layer. In both cases, the pore formation always occurs with cylinders forming perpendicular to the surface.

The mean pore sizes and their standard deviation are  $17.7 \pm 1.6$  nm with RCP and  $16.9 \pm 2.4$  nm without RCP film. The pore density is  $7.68 \times 10^{10}$  cm<sup>-2</sup> on the RCP-neutralized surface and  $7.02 \times 10^{10}$  cm<sup>-2</sup> on the untreated TiO<sub>2</sub> surface, *i.e.* the use of the RCP brush layer enhances the order in the BCP pore layer on TiO<sub>2</sub> still a bit, but not as much as in the case of SiO<sub>2</sub>. This is a very different behavior compared to the case of SiO<sub>2</sub> surfaces. Altogether, the pore density on TiO<sub>2</sub> is smaller than that on SiO<sub>2</sub>, for which we observed densities of up to  $9.4 \times 10^{10}$  cm<sup>-2</sup>. However, this demonstrates that the RCP brush is not essential for the formation of perpendicularly oriented nanopores on TiO<sub>2</sub> surfaces.

The surface free energies (SFEs) of these surfaces were determined to investigate the impact of the surface neutrality on the PMMA cylinder orientation. To this end, contact angles with the test liquids water, diiodomethane and ethylene glycole are measured on SiO<sub>2</sub> and TiO<sub>2</sub> surfaces with and without the RCP neutralization layer. The results for these surfaces and some metal thin films deposited by different PVD methods are summarized in Table 1. From these contact angles the surface free energies can be calculated by the OWRK method.<sup>52</sup> Due to the different nature of the test

liquids used, the OWRK method also allows determining the polar fraction of the surface free energy. These investigations show that SFEs vary in a narrow range between 36 and 48 mN m<sup>-1</sup> but the planar SiO<sub>2</sub> surface has with 46% a much more polar character than all other surfaces. All others are nearly completely disperse with polar fractions between 0.1 and 14%. Thus, we assume that this polar character determines the interfacial energy contribution  $F_{\text{interface}}$  to the total free energy of the BCP thin film. Due to the polar SiO<sub>2</sub> surface this surface is not neutral to PS and PMMA, leading to PMMA cylinders being parallel to the surface unless a brush layer is used. The deposition of the RCP brush layer largely reduces the polar character of the surface and therefore could promote the vertical orientation of PMMA cylinders. It is also proposed in the literature that the consideration of just the total SFE is not sufficient to describe the effect of the interfacial energy  $F_{\text{interface}}$  on the different BCP microphase separation behaviors of non-RCP-covered and -covered SiO<sub>2</sub> surfaces.<sup>20</sup> It was proposed that different polar and disperse contributions at the same total SFE lead to different BCP orientations.<sup>58</sup>

In order to verify this hypothesis we performed BCP lithography also on the metal surfaces. To this end, we deposited thin films of gold and platinum on SiO<sub>2</sub> covered Si crystals either by electron beam evaporation or by sputter deposition. The results of the BCP lithography on these surfaces are shown in Fig. 3. We found that on all the metallic surfaces PMMA cylinders are formed perpendicular to the substrate surface during microphase separation without the use of any surface neutralization film. This result clearly underlines the close relationship between a high polar fraction of the surface free energy and the orientation of PMMA cylinders parallel to the interfaces for PS-*b*-PMMA BCP lithography. At the same time it opens a new route for the creation of vertical nanopores in thin films avoiding the time consuming RCP brush layer formation steps. The demonstration of BCP lithography on the surfaces of different materials also paves the way for new applications of this nanopatterning technique. For instance, the presented nanopatterning of TiO<sub>2</sub> surfaces can not only be

**Table 1** Contact angles (CA) on different material surfaces with water, diiodomethane and ethylene glycol and calculated surface free energies (SFE) with polar fraction. The root mean square (rms) roughness of surfaces is measured by AFM. Nanopore characteristics after BCP lithography on evaporation and sputter deposited gold and platinum thin films. The corresponding data for RCP-functionalized SiO<sub>2</sub> and TiO<sub>2</sub> for comparison. Pore densities and pore sizes are determined using Delaunay based software evaluating SEM images of typically 7600 and 2700 pores, respectively. No pore diameters and densities are available for the SiO<sub>2</sub> surface as PMMA cylinders are oriented parallel to the surface. It should be noted that the polarity of the evaporated Pt films is surprisingly high. The origin of this reproducible effect, however, is beyond the scope of this paper and values are compiled as measured for the films used here

	SiO <sub>2</sub> + RCP	SiO <sub>2</sub>	TiO <sub>2</sub> + RCP	TiO <sub>2</sub>	Au <sub>evap</sub>	Au <sub>sput</sub>	Pt <sub>evap</sub>	Pt <sub>sput</sub>
CA [°]								
H <sub>2</sub> O	80	54	78	75	92	95	68	109
CH <sub>2</sub> I <sub>2</sub>	42	58	49	47	24	28	44	41
EtGly	57	42	58	53	59	67	47	55
SFE [mN m <sup>-1</sup> ]								
Polar	39	48	36	39	46	45	40	39
rms roughness [nm]	9%	46%	14%	7%	0.1%	0.1%	12%	0.2%
	0.3	0.2	0.5	0.5	0.4	5.6	0.6	1.2
Pore size [nm]	16.8 ± 2.9	—	17.7 ± 1.6	16.9 ± 2.4	18.0 ± 2.5	14.4 ± 1.7	17.4 ± 3.2	15.7 ± 2.4
Pore density [10 <sup>10</sup> cm <sup>-2</sup> ]	9.4	—	8.1	8.0	7.1	8.8	8.4	8.8

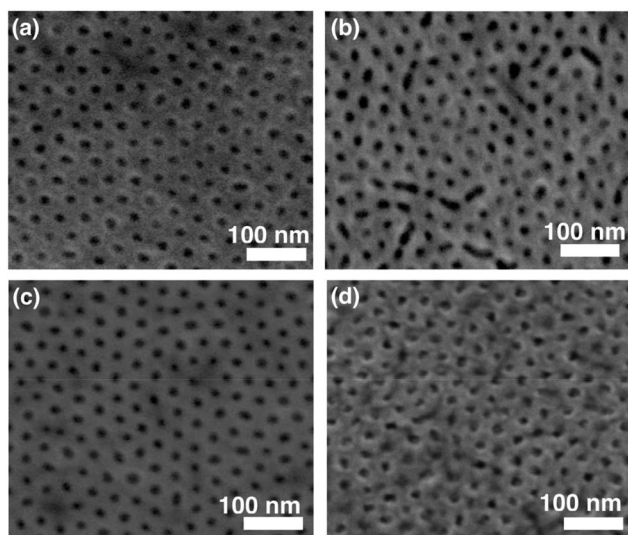


**Fig. 3** SEM images of BCP nanopores on metal surfaces without a neutralization layer. (a) Nanoporous PS on (a) an electron beam deposited Au thin film, (b) a sputter deposited Au thin film, (c) an electron beam deposited Pt and (d) a sputter deposited Pt film. Sputter deposited films have a thickness of 35 nm; evaporated films are 10 nm thick.

applied to native  $\text{TiO}_2$  on pure Ti surfaces but also on the native  $\text{TiO}_2$  on biocompatible Ti-6Al-4V surfaces.<sup>59</sup> This material is widely used in biomedical applications, *e.g.* as an implant material. Its large-area nanopatterning with defined patterns could allow for new insight into the tissue integration on the surfaces of biomedical devices.

**Influence of surface roughness.** Due to the different metal thin film preparation techniques used, we see an influence of the surface roughness on the nanopore morphology. Roughness data as well as pore sizes and densities for different substrate surfaces are compiled in Table 1. The metal thin films prepared by electron beam evaporation are very smooth, which is typical of this deposition technique. The root mean square (rms) roughness determined by AFM measurements is 0.4 nm for gold and 0.6 nm for platinum films. The BCP nanopores shown in Fig. 3(a) on a gold surface and those shown in Fig. 3(c) on a platinum surface show pore diameters and densities comparable to those on RCP neutralized  $\text{SiO}_2$  and  $\text{TiO}_2$  surfaces. The sputter deposited thin films in contrast are very rough. Film roughnesses are 5.6 nm for gold and 1.2 nm for platinum. This seems to influence the nanopore formation, as is visible in Fig. 3(b) for gold and in Fig. 3(d) for platinum. The nanopores are very irregular in shape and their average size is smaller than that on the smooth surfaces. However, the pore densities on rough sputter deposited surfaces are higher than those on the smoother oxides and electron beam evaporated metal surfaces. This indicates that under otherwise the same conditions, microphase separation is directly affected by the surface roughness.

According to the description of the total free energy  $F$  of the BCP thin film as a sum of mixing free energy, interfacial free energy and elastic energy (eqn (1)), changes of the interfacial

energy  $F_{\text{interface}}$  and the elastic energy  $F_{\text{elast}}$  may result in a slightly shifted energy minimum of the BCP thin film. The free energy  $F_{\text{mix}}$  is assumed to be constant since the same polymer is used in all experiments.

A change in the contribution of these energies to the total free energy of the polymer on the surface could result in changed characteristic properties of the homopolymer domains, here the nanopore diameter and shape.<sup>17,28</sup>

The interfacial energy between the polymer and the substrate surface is affected by the roughness as the interfacial area is increased in comparison with smooth surfaces. Thus, the influence of the polarity and surface free energy on the wettability of the surface with the polymer is likely to contribute more strongly to the total energy of the system. The influence of changes in the interfacial energy on the dimensions of the microphase separated PMMA domains is also visible when comparing nanopore diameters on smooth surfaces of different materials. The surfaces of  $\text{SiO}_2$  (RCP neutralized),  $\text{TiO}_2$  and evaporated Pt and Au all exhibit rms roughnesses below 0.6 nm. However, the mean diameters of the nanopores on these surfaces range from 16.8 nm up to 18.0 nm, as listed in Table 1. Even though this difference is small and lies within the accuracy of the measurement, it is reproducible throughout several experiments.

Different pore diameters on the same material surface but with different surface roughness are likely to result from an additional change of the elastic free energy. In order to wet the surface completely, polymer chains need to change their conformation, to follow the surface roughness. Thus polymer bonds need to get stretched or compressed, enhancing the elastic free energy. As the roughness of the investigated surfaces matches the dimensions of the radius of gyration of the BCP, which is approximately 2 nm,<sup>25</sup> a conformal arrangement of the polymer on the rough surface would result in a deformation of the PMMA cylinders. Thus, the formed nanopores would appear irregularly shaped in the top view, exhibiting a reduced diameter, as observed in our experiments.

### Block copolymer lithography in antidots

**Preparation of antidot pre-patterns.** For the formation of hierarchical nanostructures we combined block copolymer (BCP) lithography with nanosphere lithography (NSL). To this end, the  $\text{TiO}_2$ , Au and Pt thin films described above were patterned by NSL to obtain antidots, *i.e.* open volumes reaching down to the  $\text{SiO}_2/\text{Si}$  substrate. The preparation process has already been outlined in Fig. 1(a) but will be described in more detail in the following, because this is necessary to understand the results on the formation of hierarchical structures.

Monolayers of polystyrene spheres with a diameter of 618 nm are deposited onto  $\text{SiO}_2$  surfaces by convective self-assembly. The spheres arrange themselves into hexagonally close packed arrays as shown in Fig. 4(a). At present, we can fabricate monolayers of spheres on areas as large as a quarter of a 10 cm Si wafer, exceeding what we need for our experiments. Monolayers are occasionally interrupted by double-

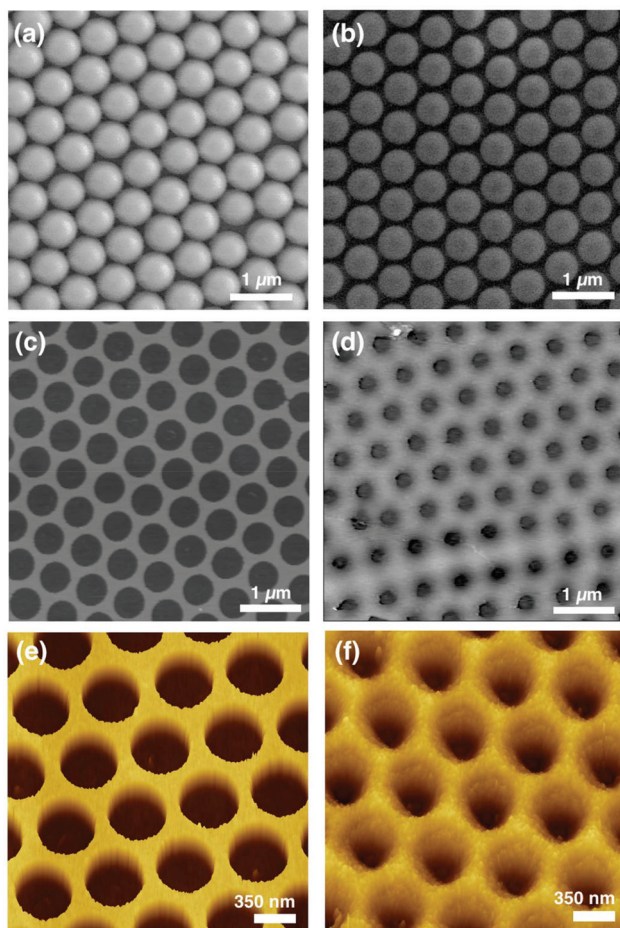


**Fig. 4** SEM and AFM images of the steps of the antidot pattern preparation. (a) Polymer sphere monolayer on a SiO<sub>2</sub> substrate. Sphere diameter is 618 nm. (b) Polymer spheres from (a) are treated in an O<sub>2</sub>-Ar plasma resulting in sphere shrinking. These shrunken spheres can act as a shadow mask in a metal deposition step. After sphere removal antidot films from the metal with hexagonally arranged free substrate areas remain. The topography of the antidot edges is determined by the metal deposition technique. (c + e) AFM images from the top view and the tilted view after platinum electron beam evaporation. (d + f) AFM images (top view + tilted) after platinum sputter deposition.

layers of spheres, their areal fraction being less than 18% according to numerical evaluations of optical interference images.<sup>60</sup> The exposure of such a polymer sphere layer to an argon-oxygen plasma results in sphere shrinking, leading to hexagonally arranged non-interconnected PS mask particles as is visible in Fig. 4(b). The diameter to which the spheres are shrunk can be controlled by the duration of the plasma process.<sup>50,53</sup>

We use these shrunken spheres as a shadow mask in nanosphere lithography. Ti, Pt and Au, respectively, are deposited onto the partially masked substrate by physical vapor deposition (PVD) techniques. The mask particles are subsequently removed, leaving a thin film of the deposited material with hexagonally arranged antidots of the free substrate. These antidot patterns are shown in the AFM images in Fig. 4(c-f).

Fig. 4(c) and (d) are in top view, and (e) and (f) in tilted 3D. A larger section of an antidot-patterned surface is presented in Fig. S1 of the ESI.†

The topography of the antidots depends strongly on the chosen PVD technique. Fig. 4(c and e) show antidots prepared by electron beam evaporation of 15 nm platinum. The antidot contour is very sharp and the side walls have a steep slope. The diameter is commensurate with the diameter of shrunken spheres. Sputter deposition of the same metal, however, leads to antidot patterns with less defined contours and less steep antidote side walls, as can be seen in Fig. 4(d and f). This is due to the less unidirectional deposition of metal atoms with the sputtering technique. Metal atoms can reach the substrate underneath the equator of the shrunken spheres; thus the diameter of the antidots is smaller than the top-view diameter of the shrunken spheres. The side wall slope is approximately 10–20°.

**BCP lithography in sputter and electron beam evaporation deposited antidots.** The antidot-patterned surfaces were used as templates for directed block copolymer lithography. Fig. 5 shows SEM images of platinum antidot films on SiO<sub>2</sub>/Si substrates after performing the BCP lithography as described before. For the antidot preparation PS spheres were shrunk from a diameter of 618 nm down to 415 nm. Platinum was then sputter deposited or electron beam evaporated (Fig. 5(a) and (b), respectively). After sphere removal, PS-*b*-PMMA dissolved in toluene was spin-coated onto the pre-patterned surfaces. No RCP-neutralization layer was used.

For both cases it is obvious in Fig. 5 that site-selective nanopore formation takes place inside the antidots. That is, microphase separation has led to vertical PMMA cylinders (which then were removed by acetic acid) inside the antidots, but not on the planar platinum thin film.

In Fig. 5(a) the rims of antidots are barely visible due to the small slope of antidot sidewalls. The free SiO<sub>2</sub> substrate areas in the center of the antidots can be observed as dark grey dots due to material contrast in the SEM. The diameters of antidots can be estimated from the overlay of SEM images (Fig. S2, ESI†) taken with an in-lens detector, in which the nanopores are visible, as in Fig. 5(a), with those of a backscattered electron detector, where the Pt gives a strong contrast. An exemplary antidot rim is marked in Fig. 5(a) (red dotted line). In the areas where BCP phase separation is clearly observed, solely cylindrical nanopores are visible which are oriented perpendicular to the substrate surface, as can be deduced from their circular shape when seen in top view. Pore diameters fit the results on planar thin films, and the hexagonal arrangement is nearly defect-free. Thus, pore densities inside the antidots are as high as  $9.2 \times 10^{10} \text{ cm}^{-2}$ . In Fig. 5(b) antidot areas are clearly visible due to the use of electron beam evaporation for the pre-patterning. Nanopores in the remaining PS film are again predominantly site-selectively formed inside the antidots and the orientation of the former PMMA cylinders is perpendicular to the substrate.

The site-selective nanopore formation inside the antidots is surprising: the antidot patterns exhibit a topographical pat-

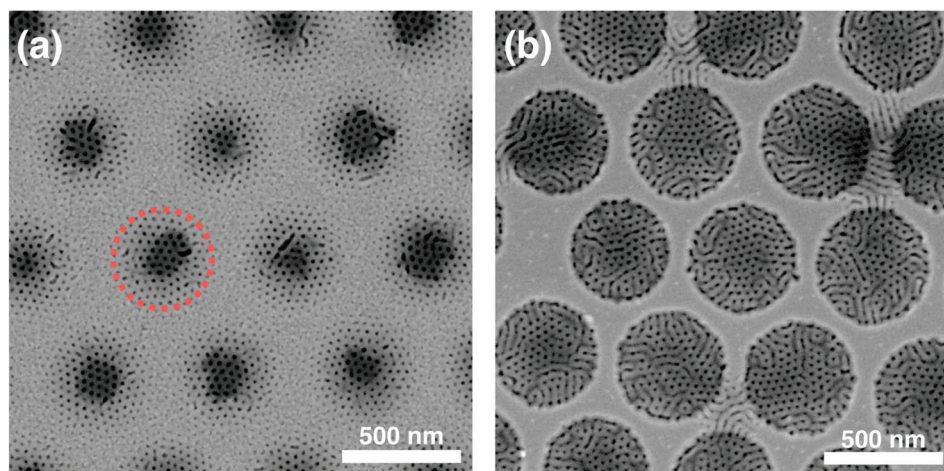


**Fig. 5** SEM images of hierarchical nanopores in polystyrene in platinum antidot patterns. (a) Antidots prepared by Pt sputter deposition (32 nm) during nanosphere lithography. The red dotted line marks the rim of an antidot. (b) Antidots in a 30 nm Pt film formed by electron beam evaporation.

tering of the substrate along with a chemical contrast between the Pt thin film and the SiO<sub>2</sub> antidot bottom. It was shown in the previous section of this paper that BCP microphase separation on planar Pt thin films, either sputter deposited or evaporated, results in the formation of perpendicularly oriented PMMA cylinders. On the antidot patterned Pt film, however, we do not observe any pore formation. However, we do observe the formation of PMMA cylinders with perpendicular orientation inside the antidots, which is particularly unexpected as the antidot bottom consists of a free SiO<sub>2</sub> surface without a RCP neutralization layer. On planar SiO<sub>2</sub> substrates, PMMA cylinders form parallel to the surface (Fig. 2(c)). On the pre-patterned antidot surfaces this is not the case.

Thus, the predominant pore orientation perpendicular to the surface is obviously guided by the topography of the antidots, both for antidots with steep (evaporated) and flat (sputter deposited) side wall slopes. Only a few horizontal pores (fingerprint-like patterns) are visible in the antidots, probably due to variations in BCP film thickness and possibly due to incomplete microphase separation. As on the planar Pt

surface between the antidots, pore containing films can be found only occasionally, the question arises whether there is any thin polymer film at all (this would not be observable in the SEM or AFM) or whether all of the polymer is inside the pores.

To answer this question we performed cross-sectional bright-field TEM (Fig. 6) on the hierarchical nanopores formed by BCP lithography on sputter deposited Pt antidot thin films, as in Fig. 5(a). A 12 nm thick Ni layer was deposited onto the sample prior to the cross-sectional TEM sample preparation in order to create a contrast between open pores and the BCP-polystyrene and prevent filling up of the pores with the glue used in specimen preparation. Fig. 6 shows that the platinum thin film sits on a silicon substrate with 4 nm native oxide and has a thickness of 32 nm. Towards the antidot center the Pt film thickness decreases and the Pt film is interrupted. It is obvious that on top of the planar part of the Pt film, there is a 8 nm thick PS film, capped by the Ni protection layer. Nanopores in the PS film can be located as Ni has penetrated into the nanopores, forming Ni nanoparticles inside the

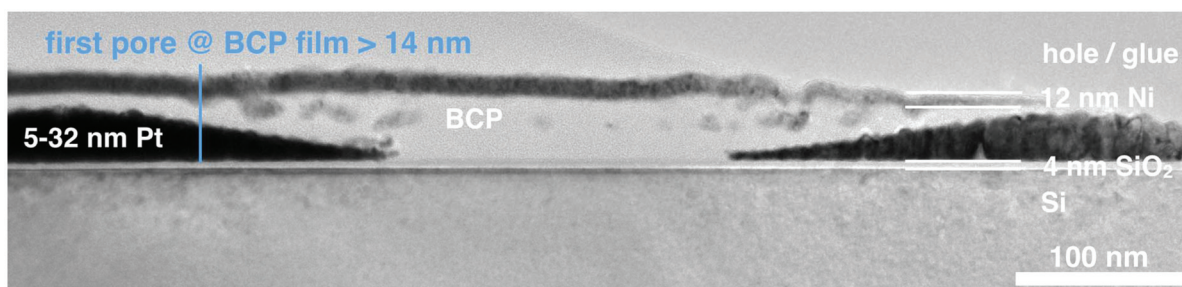


**Fig. 6** Cross-sectional bright-field TEM image of a Pt antidot formed by sputter deposition on a Si surface with 4 nm native SiO<sub>2</sub>. BCP lithography was performed on this pre-patterned surface as in Fig. 5(a). A 12 nm Ni film was deposited as a protective layer during TEM sample preparation, allowing us to observe the polymer film and pores therein. From this, the critical polymer thickness for the formation of ordered pore patterns can be determined to be 14 nm.

polymer film. The polymer film thickness increases with decreasing Pt thickness towards the antidot center. Nanopores can be found only at a polymer thickness of 14 nm or above.

It is reported in the literature<sup>18,61,62</sup> that the microphase separation only results in ordered patterns if the film thickness of the polymer is sufficiently high. This means that for very thin polymer films, microphase separation does not lead to the formation of ordered nanopores. In our experiment the critical thickness for ordered nanopore formation is obviously 14 nm.

Our observations indicate that both the material chemistry and topography of the pre-patterned surfaces contribute to the site-selective arrangement of vertical nanopores inside the antidots.

By a comparison of the sputter deposited antidot films and the evaporated antidots in Fig. 5 one can exclude a major influence of the PVD deposition technique, *i.e.* of the antidot wall slope, on the site-selective nanopore formation. In case of the evaporated antidot film with steep antidot sidewalls we assume that there is also a thin polymer film on the planar part of the Pt film. Here, the polymer film thickness jumps at the rim of antidots from a value below the critical thickness for ordered micropore formation to a value above. By this, the formation of vertical nanopores occurs selectively inside the antidots. The orientation of cylindrical pores perpendicular to the substrate observed for both, flat and steep sidewall geometries,

instead of a parallel orientation as expected for a non-pre-patterned planar SiO<sub>2</sub> surface is obviously guided by the symmetry of the antidots in the Pt metal film.

**BCP lithography in antidots from different materials: discussion of wetting behavior.** For a better understanding of the materials' influence on the ordering process and the mechanism leading to the site-selective nanopore formation we produced antidots in thin films of different materials. Instead of platinum deposition in the NSL step, gold and titanium films were electron-beam deposited, respectively, the latter leading to TiO<sub>2</sub> surfaces before the BCP lithography processing was performed. Fig. 7 summarizes the results of the BCP lithography experiments on Au antidots (a, b), Pt antidots (c, d) and TiO<sub>2</sub> antidots (e, f). The top row of Fig. 7 shows SEM images (a, c, e), the bottom row (b, d, f) the corresponding AFM images.

Gold and platinum antidots seem to have a similar effect on the BCP phase separation: for gold antidots BCP nanopores are visible mainly inside the antidots as shown in the SEM image in Fig. 7(a). Here, the perpendicular PMMA cylinder orientation and the nanopore arrangement are even more homogeneous than for the Pt films (Fig. 7(c)). In the Au antidot center (excluding the outermost ring of pores), the order of pores is remarkably high and pore densities within the antidots are about  $9.4 \times 10^{10} \text{ cm}^{-2}$ , matching the geometrical maximum ( $9.43 \times 10^{10} \text{ cm}^{-2}$ ). Defects in pore morphology

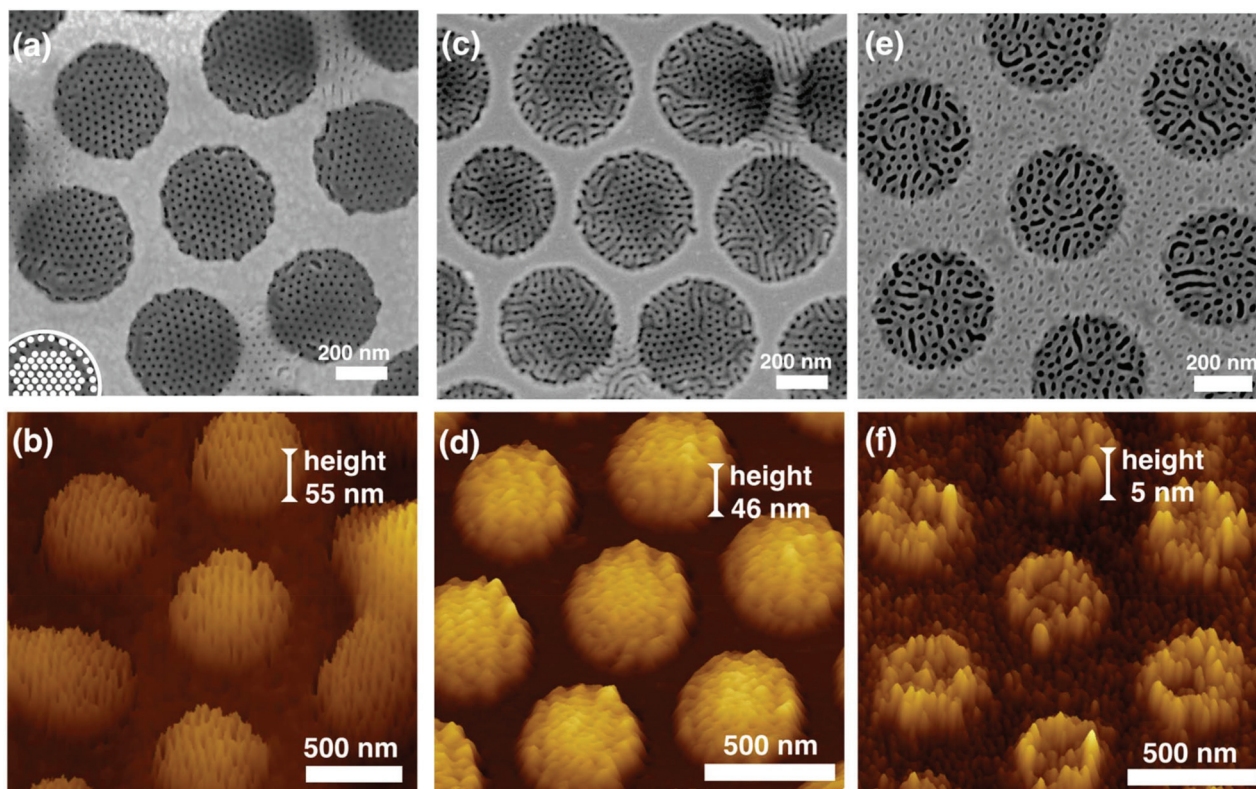


**Fig. 7** Top-view SEM images of the pore structure (top row) and tilted AFM (bottom row) images showing the topography of nanoporous PS in antidots prepared by electron beam deposition of different materials. (a, b) Antidots in a Au film, (c, d) in a Pt film, and (e, f) in a TiO<sub>2</sub> film. The schematics in (a) illustrates the deviating pore ordering near the rim of antidots, for clarity in an exaggerated form.

only occur at the antidot rim, where the pore arrangement follows the antidot shape, *i.e.* deviations of the antidot rim from a perfect circularity are represented by a commensurate arrangement of the outer circle of pores. Between this outer circle of pores and the rim walls there is always a thin film of PS left. This indicates that the antidot walls are preferentially wetted with PS rather than with PMMA. The distance between this outer circle of pores and the next pore row is often larger than the regular center–center distance between pores apparent in the antidot center where pores arrange themselves in perfect order. Thus, one can assume that the microphase separation starts in the antidot center and is disturbed only when approaching the antidot wall in a distance not commensurate with the pattern periodicity. In a few areas nanopore formation also occurs in between the antidots on the metal film. We assume that a polymer film, invisible in the SEM as long as there is no microphase separation, is present on the entire top surface of the Au film, similar to the thin polymer film we observed on the Pt antidots in Fig. 6. However, a locally higher surface roughness could lead to a better wettability and thus a locally higher BCP film thickness. It is likely that microphase separation occurs only at these small patches exhibiting a suitable polymer thickness.

The BCP lithography on an antidot patterned titanium oxide surface, Fig. 7(e), shows very different results. The nanopore formation occurs all over the surface, *i.e.* inside the antidots and on the planar surface areas in between. Moreover, the pore size distribution is much broader than for the site-selective pores in Au and Pt antidots. Obviously, in the case of the TiO<sub>2</sub> antidot films the largest pores occur in the antidots. The broad size distribution could be due to several reasons. One could explain this to be a result of unfinished microphase separation or an incommensurate polymer film thickness. Most likely it is completely due to the nature of materials in contact with the BCP and the topography of the surface: at the bottom of antidots, the surface consists of SiO<sub>2</sub> where in the absence of a RCP brush layer BCP shows a strong tendency for in-plane cylinder arrangement (Fig. 2(d)). The antidot side walls consist of TiO<sub>2</sub>, on which BCP tends to form vertical PMMA cylinders upon phase separation (see Fig. 2(f)), *i.e.* cylinders vertical to the side walls. On the planar TiO<sub>2</sub> top surface the PMMA cylinders are expected to align vertically as well. From this one would expect that PMMA cylinders should tilt at the upper rim of an antidot from vertical at the planar top surface to horizontal inside the antidot. This, however, is not observed, indicating that, in addition, a gradient in the polymer thickness near the antidot rims determines the ordering of PMMA cylinders.

A good wettability of TiO<sub>2</sub> with the polymer, *i.e.* a low interfacial energy between TiO<sub>2</sub> and BCP dissolved in toluene, allows for the deposition of polymer with a sufficiently large film thickness on the planar areas between the antidots, resulting in the overall formation of nanopores. In contrast, a poor wettability of the metal surfaces results in a low film thickness on the planar areas between the antidots and thus in the site-selective nanopore formation exclusively inside the antidots. In order to check this assumption, we made a test

sample with antidots from 33 nm electron beam evaporated titanium oxide and subsequently deposited 5 nm of platinum by sputtering. This means that the topography is the same as the one in Fig. 7(e), but the top-surface is covered with a sputter deposited Pt film instead of an evaporated TiO<sub>2</sub> film. Performing the BCP lithography on such a surface again results in the site-selective pore formation inside antidots (Fig. S3, ESI†), similar to the Pt antidot film in Fig. 7(c). This experiment supports the conclusion that depending on the antidot material the BCP film thickness varies between the inner and outer section of the antidots to a different extent, leading to either site-selective or uniform arrangement of vertical nanopores in or on antidot films.

For a better understanding of the morphology of the hierarchically patterned antidot structures we performed AFM measurements (Fig. 7(b, d and f)). To our surprise the nanoporous PS matrix forms elevated domes on the antidots. In the case of the noble metal antidot films these domes are very distinct. They have heights of 55 nm for Au (Fig. 7(b)) and 46 nm for Pt (Fig. 7(d)) with respect to the flat top surface level. Elevated domes are visible on TiO<sub>2</sub> antidot films, too; however their height reaches only about 5 nm. The pronounced roughness measured by AFM on the flat top TiO<sub>2</sub> areas (Fig. 7(f)) reflects the formation of nanopores in the polymer film between the nanopores.

The formation of domes occurs during annealing of the BCP film. AFM measurements of evaporated Au antidots spin coated with BCP prior to annealing do not show a dome on antidots, but a polymer film with a regular array of dimples covering the surface. From the reduction of antidot depth one can see that a larger amount of BCP is deposited inside the antidots than outside (Fig. S4, ESI†). We assume that during the annealing, residual solvent from the BCP spin coating process evaporates. Due to the topography and the larger amount of polymer inside the antidots than on the planar top areas, it is likely that more solvent is trapped inside the antidots, pushing the BCP film up during annealing. This is particularly pronounced for Au and Pt films, because the difference in BCP film thickness in the antidots and on the planar top surface is larger than in the case of the TiO<sub>2</sub> antidot films. Thus dome formation on TiO<sub>2</sub> antidot films is small. This thesis is further supported by the fact that dome formation on sputter-deposited antidots is present but small (10 nm dome height on sputter-deposited platinum antidots in Fig. 5(a)) as the volume of these antidots with a small wall slope is smaller than the volume of electron beam deposited antidots with steep walls. Thus, less polymer and less solvent are trapped here. The dome formation corresponds to a local delamination of the BCP film inside the antidots. The presence of a cavity underneath the domes can also be concluded from geometrical considerations (see the ESI†).

Such a local delamination of the polymer film off the substrate could also contribute to the perpendicular PMMA cylinder orientation inside the antidots, which was surprising since the antidot bottom consists of non-neutralized SiO<sub>2</sub> on which a parallel cylinder orientation would be expected from experi-

ments on planar surfaces. A polymer film which is pushed away from the surface would not contact the SiO<sub>2</sub> surface at the bottom of the antidots but form a free-standing film above the antidots. Thus, two interfaces with air are formed, which are neutral towards the polymers and allow for the perpendicular nanopore formation.

## Conclusions

In this paper, we present the self-organized formation of hierarchical nanopores using a combination of nanosphere lithography and block copolymer lithography. In order to understand BCP lithography with cylinder forming PS-*b*-PMMA on pre-patterned surfaces from different materials, we first performed BCP lithography on planar surfaces of SiO<sub>2</sub>, TiO<sub>2</sub>, Au and Pt. We demonstrated the creation of ordered nanopores on these material surfaces – to our knowledge for the first time – which largely expands the range of possible applications of BCP lithography. The patterning of TiO<sub>2</sub>, for instance, is not only applicable to native TiO<sub>2</sub> on a Ti layer but also to the native oxide on Ti-6Al-4V alloy surfaces (to be published elsewhere), which is interesting for biomedical applications.

We investigated the surface free energies of the different material surfaces and found that the polar fraction of the SFE determines the pore orientation. A high polar fraction as in SiO<sub>2</sub> leads to cylinder orientations parallel to the surface, resulting in the need for neutralization layers, such as RCP brushes in order to obtain vertically oriented cylinders. On the other hand, on disperse surfaces such as Au, Pt or TiO<sub>2</sub> neutralization layers are not required to achieve vertical nanopores by applying different PVD techniques for the creation of metal thin films, we demonstrate that surface roughnesses influence the characteristic dimensions of the block copolymer nanopores, *i.e.* nanopore diameter, density and shape.

For the creation of hierarchical nanopores, we patterned thin films of these materials (Au, TiO<sub>2</sub>, and Pt) by means of nanosphere lithography with antidots, *i.e.* arrays of cylindrical holes in the thin films, providing topographical and chemical surface patterns, for directed BCP self-assembly. We demonstrate that the combination of these self-assembly techniques allows for the creation of vertical nanopores formed site-selectively inside antidots in metal films, *i.e.* hierarchical cylinder-in-cylinder patterns. The use of sputter deposition and electron beam evaporation for the creation of the antidot patterns allowed us to exclude the influence of the antidot wall slope on the site-selectivity. Cross-sectional TEM investigations indicate a dependence of the nanopore formation on the polymer thickness, which varies due to the inhomogeneous wetting on of the patterned surface. This effect also becomes obvious using different materials for the antidot thin films: we found site-selective nanopores for poorly wettable metal surfaces and surface covering nanopores for homogeneously wetted TiO<sub>2</sub> surfaces. AFM measurements show that the nanoporous PS forms elevated domes on the antidots. We discuss that these domes evolve due to solvent evaporation upon BCP annealing.

This results in locally free-standing polymer films with two interfaces towards the air at the antidots, contributing to the observed perpendicular cylinder orientation in these films by matching the SFE conditions as investigated on planar material surfaces.

In summary, the combination of two low-cost techniques nanosphere lithography and block copolymer lithography allows for the guided large-area nanopatterning of surfaces with hierarchical nanopores. It proved to be a flexible approach as it is applicable to several substrate materials, opening up a broad range of possible applications. As such we foresee *e.g.* the controlled surface placement of both biomolecules and quantum dots in devices exploiting the plasmonic properties of the antidot structures. Other applications may profit from the hierarchical order and improved mechanical stability involved, *e.g.* in advanced filtration techniques, but the range of application possibilities is yet to be explored.

## Conflicts of interest

All authors state that there are no conflicts to declare.

## Acknowledgements

The authors would like to thank Prof. Dr Mirco Schaper, Dept. of Mechanical Engineering, Paderborn University, for access to the SEM and M. Sc. Alexander Taube for assistance.

Dennis Drude, Dept. of Physics, Paderborn University, is gratefully acknowledged for the implementation of the Delaunay algorithm for SEM image analysis. Financial support from the DFG program GRK1464 and the Graduate School Fortschrittsskolleg LEM of the Federal State of North Rhine-Westphalia is also gratefully acknowledged.

## References

- 1 R. A. Puglisi, *J. Nanomater.*, 2015, **2015**, 586458.
- 2 H.-C. Kim, S.-M. Park and W. D. Hinsberg, *Chem. Rev.*, 2010, **110**, 146.
- 3 J. Y. Cheng, C. A. Ross, V. Z. H. Chan, E. L. Thomas, R. G. H. Lammertink and G. J. Vancso, *Adv. Mater.*, 2001, **13**, 1174.
- 4 K. Naito, H. Hieda, M. Sakurai, Y. Kamata and K. Asakawa, *IEEE Trans. Magn.*, 2002, **38**(5), 1949.
- 5 H. Tsai, H. Miyazoe, A. Vora, T. Magbitang, N. Arellano, C. C. Liu, M. J. Maher, W. J. Durand, S. J. Dawes, J. J. Bucchignano, L. Gignac, D. P. Sanders, E. A. Joseph, M. E. Colburn, C. G. Willson, C. J. Ellison and M. A. Guillorn, *Proc. SPIE*, 2016, **9779**, 977910.
- 6 W. A. Lopes and H. M. Jaeger, *Nature*, 2001, **414**, 735.
- 7 H. C. Kim, X. Jia, C. M. Stafford, D. H. Kim, T. J. McCarthy, M. Tuominen, C. J. Hawker and T. P. Russell, *Adv. Mater.*, 2001, **13**, 795.

- 8 M. Park, C. Harrison, P. M. Chaikin, R. A. Register and D. H. Adamson, *Science*, 1997, **276**, 1401.
- 9 R. R. Li, P. D. Dapkus, M. E. Thompson and W. G. Jeong, *Appl. Phys. Lett.*, 2000, **76**, 1689.
- 10 P. J. Flory, *J. Chem. Phys.*, 1942, **10**, 51.
- 11 M. L. Huggins, *J. Chem. Phys.*, 1941, **9**(5), 440.
- 12 A. Menshikov, A. V. Bolshakova and I. V. Yaminskii, *Prot. Met. Phys. Chem. Surf.*, 2009, **45**(3), 295.
- 13 P. J. Flory, *Principles of Polymer Chemistry*, Cornell Univ. Press, 1953.
- 14 F. Ferrarese Lupi, T. J. Giammaria, G. Seguini, F. Vita, O. Francescangeli, K. Sparnacci, D. Antonioli, V. Gianotti, M. Laus and M. Perego, *ACS Appl. Mater. Interfaces*, 2014, **6**, 7180.
- 15 K. W. Guarini, C. T. Black and S. H. I. Yeung, *Adv. Mater.*, 2002, **14**(18), 1290.
- 16 I. A. Zucchi, E. Poliani and M. Perego, *Nanotechnology*, 2010, **21**, 185304.
- 17 A. Andreozzi, E. Poliani, G. Seguini and M. Perego, *Nanotechnology*, 2011, **22**, 185304.
- 18 X. Zhang, B. C. Berry, K. G. Yager, S. Kim, R. L. Jones, S. Satija, D. L. Pickel, J. F. Douglas and A. Karim, *ACS Nano*, 2008, **2**(11), 2331.
- 19 S. Ham, C. Shin, E. Kim, D. Y. Ryu, U. Jeong, T. P. Russell and C. J. Hawker, *Macromolecules*, 2008, **41**, 6431.
- 20 C. K. Shelton and T. H. Epps, *Macromolecules*, 2015, **48**, 4572.
- 21 P. W. Majewski and K. G. Yager, *Soft Matter*, 2016, **12**, 281.
- 22 B. H. Sohn and S. H. Yun, *Polymer*, 2002, **43**, 2507.
- 23 R. D. Peters, X. M. Yang, T. K. Kim, B. H. Sohn and P. F. Nealey, *Langmuir*, 2000, **16**, 4625.
- 24 J. Bang, J. Bae, P. Löwenhielm, C. Spiessberger, S. A. Given-Beck, T. P. Russell and C. J. Hawker, *Adv. Mater.*, 2007, **19**, 4557.
- 25 K. Sparnacci, D. Antonioli, V. Gianotti, M. Laus, F. Ferrarese Lupi, T. J. Giammaria, G. Seguini and M. Perego, *ACS Appl. Mater. Interfaces*, 2015, **7**, 10944.
- 26 F. Ferrarese Lupi, T. J. Giammaria, G. Seguini, M. Ceresoli, M. Perego, D. Antonioli, V. Gianotti, K. Sparnacci and M. Laus, *J. Mater. Chem. C*, 2014, **2**, 4909.
- 27 H. Liu, C. T. O'Mahony, F. Audouin, C. Ventura, M. Morris and A. Heise, *Macromol. Chem. Phys.*, 2012, **213**, 108.
- 28 E. Han, K. O. Stuen, Y.-H. La, P. F. Nealey and P. Gopalan, *Macromolecules*, 2008, **41**, 9090.
- 29 S.-J. Jeong, J. Y. Kim, B. H. Kim, H. S. Moon and S. O. Kim, *Mater. Today*, 2013, **16**(12), 468.
- 30 M. Li and C. K. Ober, *Mater. Today*, 2006, **9**(9), 30.
- 31 P. Mansky, Y. Liu, E. Huang, T. P. Russell and J. C. Hawker, *Science*, 1997, **275**, 1458.
- 32 I. Bitá, J. K. W. Yang, Y. Sik Jung, C. A. Ross, E. L. Thomas and K. K. Berggren, *Science*, 2008, **321**, 939.
- 33 S. O. Kim, *Soft Matter*, 2013, **9**, 2780.
- 34 H. Hu, M. Gopinadhan and C. O. Osuji, *Soft Matter*, 2014, **10**, 3867.
- 35 A. Tavakkoli, S. M. Nicaise, K. R. Gadelrab, A. Alexander-Katz, C. A. Ross and K. K. Berggren, *Nat. Commun.*, 2016, **7**, 10518.
- 36 S.-M. Park, B. C. Berry, E. Dobisz and H.-C. Kim, *Soft Matter*, 2009, **5**, 957.
- 37 L. Rockford, *Phys. Rev. Lett.*, 1999, **82**, 2602.
- 38 R. A. Segalman, H. Yokoyama and E. J. Kramer, *Adv. Mater.*, 2001, **13**(15), 1152.
- 39 S. O. Kim, *Nature*, 2003, **424**, 411.
- 40 R. Ruiz, H. Kang, F. A. Detcheverry, E. Dobisz, D. S. Kercher, T. R. Albrecht, J. J. de Pablo and P. F. Nealey, *Science*, 2008, **321**, 936.
- 41 Q.-Y. Tang and Y.-Q. Ma, *Soft Matter*, 2010, **6**, 4460.
- 42 J. C. Hulteen and R. P. Van Duyne, *J. Vac. Sci. Technol., A*, 1995, **13**(3), 1553.
- 43 A. S. Dimitrov and K. Nagayama, *Langmuir*, 1996, **12**, 1303.
- 44 X. Ye and L. Qi, *Nano Today*, 2011, **6**, 608.
- 45 S.-M. Yang, S. G. Jang, D.-G. Choi, S. Kim and H. K. Yu, *Small*, 2006, **2**(4), 458.
- 46 Y. Li, G. Duan, G. Liu and W. Cai, *Chem. Soc. Rev.*, 2013, **42**, 3614.
- 47 H. Zhang, M. Liu, F. Zhou, D. Liu, G. Liu, G. Duan, W. Cai and Y. Li, *Small*, 2015, **11**(7), 844.
- 48 D. Gogel, M. Weinl, J. K. N. Lindner and B. Stritzker, *J. Optoelectron. Adv. Mater.*, 2010, **12**(3), 740.
- 49 A. Plettl, F. Enderle, M. Saitner, A. Manzke, C. Pfahler, S. Wiedemann and P. Ziemann, *Adv. Funct. Mater.*, 2009, **19**, 3279.
- 50 D. Kraus, J. K. N. Lindner and B. Stritzker, *Nucl. Instrum. Methods Phys. Res.*, 2007, **257**, 455.
- 51 T. Riedl, M. Strake, W. Sievers and J. K. N. Lindner, *Mater. Res. Soc. Symp. Proc.*, 2014, **1663**, mrsf13-1663-ww03-75.
- 52 M. Wahle, K. Brassat, J. Ebel, J. Bürger, J. K. N. Lindner and H.-S. Kitzerow, *Opt. Express*, 2017, **25**(19), 22608.
- 53 A. A. Rüdiger, K. Brassat, J. K. N. Lindner, W. Bremser and O. I. Strube, *Langmuir*, 2018, **34**, 4264.
- 54 B. J. Kim, D. H. Lee, J. Y. Kim, D. O. Shin, H. Y. Jeong, S. Hong, J. M. Yun, C. M. Koo, H. Lee and S. O. Kim, *Adv. Mater.*, 2011, **23**, 5618.
- 55 D. K. Owens and R. C. Wendt, *J. Appl. Polym. Sci.*, 1969, **13**, 1741.
- 56 T. M. Liebling, *Doc. Math.*, 2012, **1**, 419.
- 57 D. T. Lee and B. L. Schachter, *Int. J. Comput. Inf. Sci.*, 1980, **9**(3), 219.
- 58 E. Han, K. O. Stuen, M. Leolukman, C.-C. Liu, P. F. Nealey and P. Gopalan, *Macromolecules*, 2009, **42**, 4896.
- 59 K. Brassat, *et al.*, to be published.
- 60 J. K. N. Lindner, *et al.*, to be published.
- 61 A. Knoll, A. Horvat, K. S. Lyakhova, G. Krausch, G. J. A. Sevink, A. V. Zvelindovsky and R. Magerle, *Phys. Rev. Lett.*, 2002, **89**(3), 035501.
- 62 J. N. L. Albert and T. H. Epps, *Mater. Today*, 2010, **13**(6), 24.